Hindawi
International Journal of RF and Microwave Computer-Aided Engineering
Volume 2023, Article ID 9958074, 11 pages
https://doi.org/10.1155/2023/9958074

Research Article

Design of Broadband and Ultra-Wide-Angle Low-RCS Open-Ended Cavity Based on Phase Cancellation

Qingting He,[1] **Haiyan Chen**,[1] **Qian Liu**,[1] **Xin Yao**,[1] **Fengxia Li**,[2] **Difei Liang**,[1] **Jianliang Xie**,[1] **and Longjiang Deng**[1]

[1]*National Engineering Research Center of Electromagnetic Radiation Control Materials, Key Laboratory of Multi-Spectral Absorbing Materials and Structures of Ministry of Education, State Key Laboratory of Electronic Thin Films and Integrated Devices, University of Electronic Science and Technology of China, Chengdu 611731, China*
[2]*School of Physics, Xidian University, Xi'an 710071, China*

Correspondence should be addressed to Haiyan Chen; chenhy@uestc.edu.cn

Received 23 July 2023; Revised 23 October 2023; Accepted 31 October 2023; Published 15 November 2023

Academic Editor: Giacomo Muntoni

In this paper, it is proposed to employ phase cancellation metasurface (PCM) to substantially reduce the RCS of an electrically large open-ended cavity (EOC) by scattering the energy to the nonthreatening region, achieving broadband and ultra-wide-angle RCS reduction of the cavity. The PCM, constituted by the collection of polarizing reflectors, is loaded on the inner and outer walls of the composed cavity structure in accordance with the orthogonality principle to obtain a low-RCS cavity. The main benefits of using the polarizing reflector to build a PCM are as follows: On the one hand, it reduces the number of units that make up the PCM, which in principle only requires half of the quantity. On the other hand, it is possible to form a phase difference of 180 degrees that is completely stable. Both the simulation and measured results show that the RCS reduction of 10 dB for normal incidence relative to the original state of the cavity (that is, the metal cavity) over a frequency range of 6.3 GHz to 13.2 GHz under TE polarization and 7.8 GHz to 13.4 GHz under TM polarization has been obtained. Furthermore, the RCS reduction performances of the cavity loaded with the composed PCM under variable azimuth angles are also studied. Numerical and experimental results demonstrate that the ultra-wide-angle RCS reduction from -180° to 180° is acquired. To the best of our knowledge, this is the first time that the PCM, which is made up of a number of polarizing reflectors, has been used to get broadband and ultra-wide-angle RCS reduction for the EOC. This method, which is simple, effective, and low cost, has great application prospects in the RCS reduction design of the cavity.

1. Introduction

Radar cross-section (RCS) can be used to evaluate a flight vehicle's electromagnetic system's performance [1, 2]. By reducing the RCS of aircraft vehicles, the probability of them being detected and tracked can be reduced, thereby enhancing their survivability [3]. The electrically large open-ended cavity (EOC) structure of the aircraft, which includes the jet engine inlet ducts, nozzle, and cockpit [4–8], is a major scattering source that contributes significantly to the RCS of the target. Hence, it is crucial to achieving the RCS reduction of the EOC, which can significantly decrease the aircraft's backward electromagnetic scattering and improve the target's battlefield survivability.

Currently, the major methods for reducing the RCS of the cavity involve shaping techniques [9–13] and loading absorbing material [14–20]. For shaping technology, the strong scattering source can be converted into a weak one by designing the target's shape, thereby effectively reducing its RCS. However, it has a significant impact on the aircraft's mechanical strength and aerodynamic performance. With regard to absorbing material, the mechanism transforms electromagnetic energy into heat via electric loss or magnetic loss, which reduces the scattering energy of the cavity. It benefits from being thin and simple to repair and assemble. However, absorbing materials are typically expensive and tend to fail at high temperatures. The metasurface offers a novel technique for RCS reduction that distributes energy

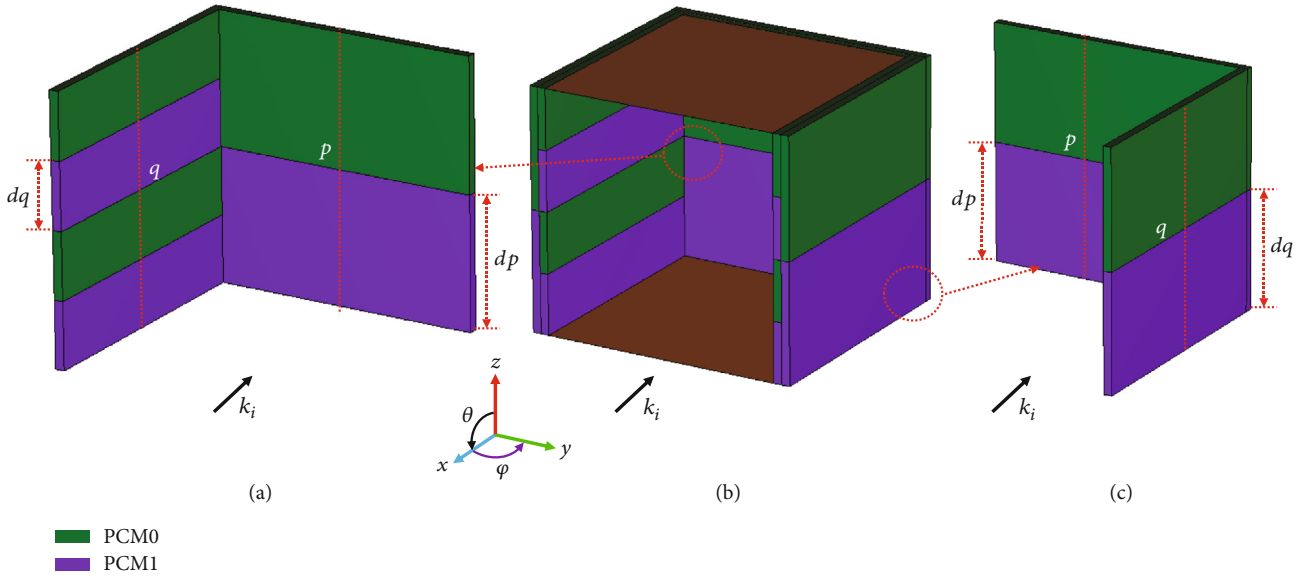

FIGURE 1: The working principle diagram of the low-RCS cavity: (a) the interior of the cavity; (b) the cavity; (c) the exterior of the cavity.

in the direction away from the threat by manipulating the wavefront [21–32]. However, metasurfaces are relatively rarely used to regulate the scattering of cavities [23]. Zhou et al. presented a novel approach to lowering the RCS of the EOC by employing metasurfaces with random distribution cross-like patterns [23]. In the X-band, they achieved the RCS reduction of the cavity from 10° to 80° incidence using the principle of diffuse reflection. The phase cancellation metasurface (PCM), which is constituted by a set of polarizing reflectors, offers excellent RCS reduction performance as one of the main metasurfaces. By creating a broadband and efficient polarization reflector and then rotating it 90 degrees, a unit cell with the same amplitude as the original unit and a 180° phase difference can be obtained. After that, the units before and after rotation are arranged alternately or placed in a checkerboard pattern to accomplish effective RCS reduction. Despite extensive research on PCM [28–32], there has been no research on the application of PCM to the field of EOC's RCS reduction, according to our investigation.

In this research, we present the design concepts and methods for controlling the scattering characteristics of the EOC by employing PCM technology. The PCM, which is made up of a group of polarizing reflectors, is applied to the inner and outer walls of the cavity structure based on array theory and the orthogonality principle. Both simulations and measurements confirm that the proposed low-RCS EOC has excellent RCS control under normal incidence from 6.3 GHz to 13.2 GHz under TE polarization and 7.8 GHz to 13.4 GHz under TM polarization, wherein the RCS reduction is greater than 10 dB and exceeds -20 dB at multiple resonant frequencies. The simulated and measured results are in good agreement over the entire frequency range. Additionally, the RCS reduction properties of the cavity loaded with the PCM are also evaluated at various azimuth angles. The reduction of the ultra-wide-angle RCS from -180° to 180° is acquired, according to numerical and experimental data. The approach employed here provides a strategy for the design of the cavity's RCS reduction.

2. Modeling, Simulation, and Discussion

Typically, a construction with an open end and a terminal metal plate can be used to represent EOC. Due to the existence of many corner reflectors in the cavity, the incident wave generates a strong backward echo after multiple reflections inside the cavity and a single reflection outside the cavity, resulting in a strong backward RCS of the cavity. To realize the backward RCS reduction of the cavity, it is necessary to design from the inside and outside of the cavity at the same time to destroy the corner reflector structure, which prevents the incident wave from forming severe echo scattering. The strong echo scattering of the corner reflector can be effectively eliminated by redirecting the electromagnetic wave away from the backscattering. The development of polarization conversion metasurfaces offers powerful support for putting this strategy into practice. The unit cell of PCM is reasonably arranged using the orthogonality principle to effectively regulate the scattering of electromagnetic waves. Then, the backward echo can be dispersed to non-threatening areas by loading PCM on the cavity's inner and outer walls.

As previously explained, due to the existence of corner reflectors in the cavity, the plane wave generates a strong backward echo after multiple reflections in the cavity and a single reflection outside the cavity. To reduce the RCS of the cavity, it is necessary to disrupt the corner reflector structure to prevent the incident plane wave from causing severe echo scattering. This can be attained by applying destructive interference to cancel the scattering, according to the array theory [21]. The typical method is to employ two PCMs with a 180° phase difference. Figure 1 shows the working principle diagram of the low-RCS cavity. As shown in Figure 1, the phase difference between PCM1 and PCM2

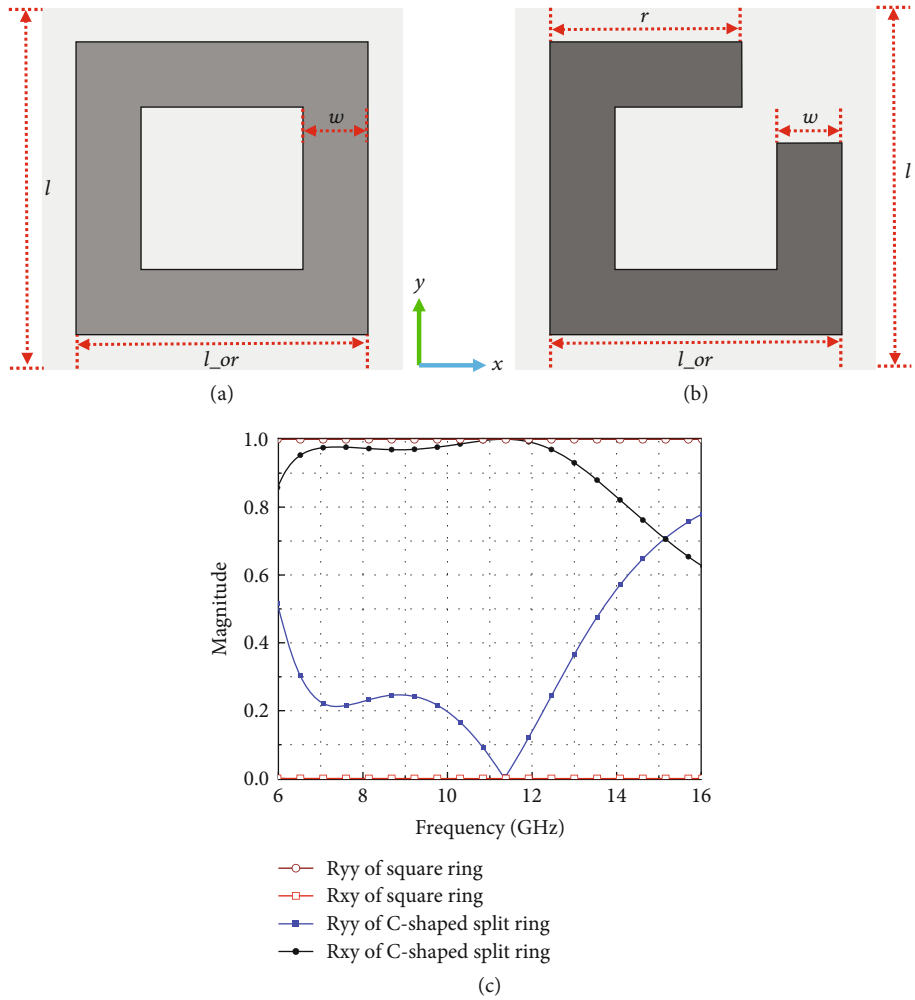

FIGURE 2: The schematic illustration of the (a) square ring unit cell and (b) C-shaped split-ring unit cell. (c) Reflection of cross-polarization Rxy and co-polarization Ryy of the square ring unit cell and the C-shaped split-ring unit cell.

is 180 degrees. Then, according to the principles of orthogonality theory, the interior and exterior of the cavity are designed according to the following method [33]. The schematic diagram of the cavity's internal and external working principles is shown in Figures 1(a) and 1(c), respectively. Figure 1(b) shows the schematic diagram of the whole cavity. To prevent the emergence of grating lobes in the region parallel to the plane of incidence, the array axis is designed to be perpendicular to the incident plane so as to regulate the lobes to the nonthreat area [33], that is,

$$p//q//(k_i \times n), \tag{1}$$

where p and q stand for the array axes, k_i is the incidence wave vector, and n represents the incident plane's normal vector.

For the interior of the cavity, as shown in Figure 1(a) [33],

$$dp = M * dq, M = 2 * m. \tag{2}$$

For the external of the cavity, as seen in Figure 1(c) [33],

$$dp = N * dq, N = 2 * m - 1, \tag{3}$$

where dq and dp are the periods of the supercell and the value of m is 1,2,3...

As previously stated, the unit cell of the PCM with a 180° phase difference is necessary to reduce the cavity's RCS. Considering the performance of wideband RCS reduction, the polarizing reflector as the unit cell of the PCM has many benefits. The main advantages of using the polarizing reflector to construct a PCM are as follows: Firstly, it reduces the number of units that make up the PCM, typically requiring only half of the quantity. Secondly, a stable 180° phase difference can be created. At first, a square ring is chosen as the pattern of the unit cell, as seen in Figure 2(a). The unit cell is a classical sandwich structure. The pattern on the top is silver. The ground plane is made of aluminum. The dielectric separator is air with a thickness of 5.5 mm. Using CST Microwave Studio with the frequency domain solver, the boundary condition is set as unit cell boundary in both x- and y- directions and open (add space) boundary in the z

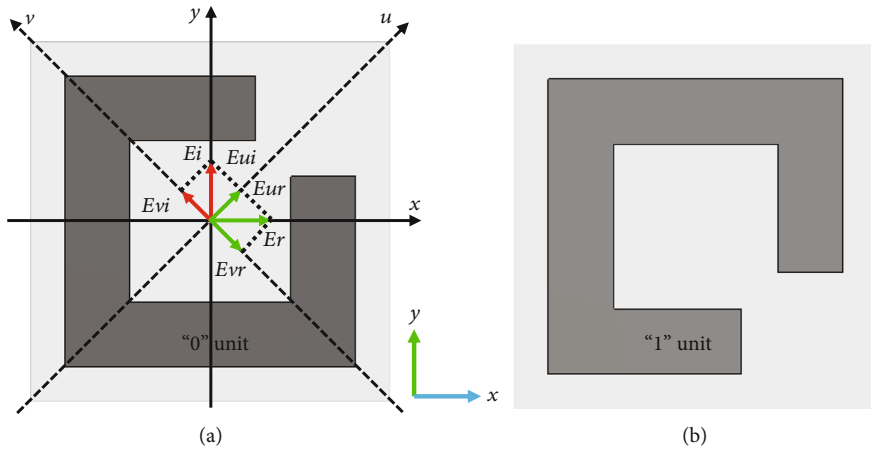

FIGURE 3: The working principle of the unit cell of PCM and the schematic illustration of the (a) "0" unit and (b) "1" unit.

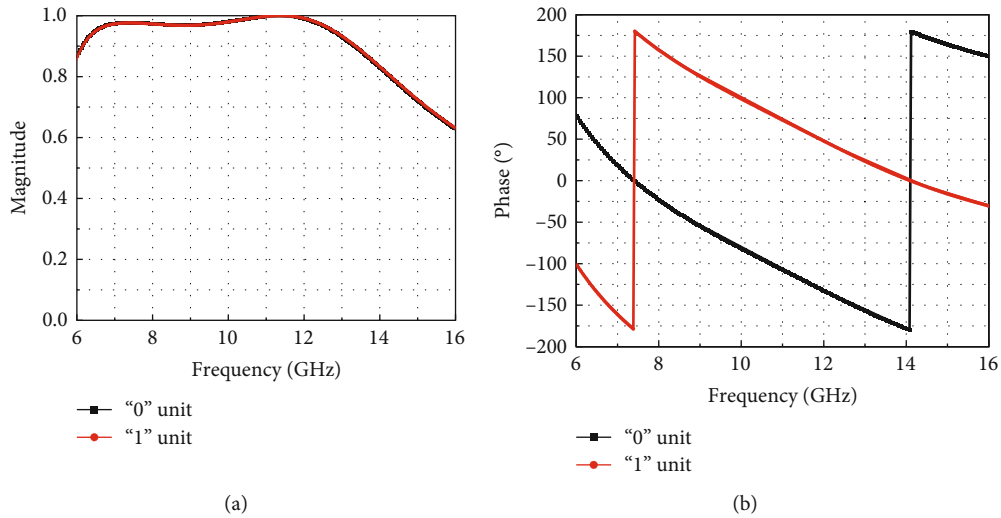

FIGURE 4: (a) The cross-polarized reflection coefficient and (b) the cross-polarized reflection phase of "0" and "1" units.

direction; the parameters of the element are optimized. The geometrical parameters are $l\_or = 8.1$ mm, $w = 1.8$ mm, and $l = 10$ mm. Only copolarized components dominate because the structure is not anisotropic and the cross-polarized magnitude is nearly 0, which is fairly apparent as can be seen in Figure 2(c). To introduce anisotropy and produce higher cross-polarized components Rxy, the C-shaped split-ring pattern is formed by truncating the corners of the square rings, as shown in Figure 2(b) [28]. The optimized geometrical parameters are $r = 5.3$ mm, $l\_or = 8.1$ mm, $w = 1.8$ mm, and $l = 10$ mm. As can be observed from Figure 2(c), the cross-polarized components Rxy are significantly improved as a result of the introduced asymmetry in the pattern of the unit cell. The split-ring structure has the advantages of high anisotropy, flexible design, and simple manufacture [34]. Therefore, we select the C-shaped split-ring pattern as the polarized reflector, and the working principle of the polarization converter to realize polarization conversion is shown in Figure 3(a) [28, 31]. For clearer analysis, we created the x - y coordinate system and the u - v coordinate system, which are formed by turning the x - y coordinate system 45 degrees anticlockwise. Suppose that the electromagnetic wave is impacting the unit along the y -polarization, we express the electric field as *Eyi*. The electromagnetic wave can be decomposed into two orthogonal components, *Eui* and *Evi*, in accordance with the vector decomposition theory. The element displays perfect magnetic conductor properties in the u direction, which causes the electric field components *Eur* and *Eui* of the reflected wave to be in phase. However, since the element displays perfect magnetic conductor properties in the v direction, the reflected wave electric field components *Evr* and *Evi* in this direction are opposite. Therefore, in accordance with the vector synthesis principle, the reflected wave electric field is along the x axis, which is *Exr*. Namely, after the electric field direction of the incident wave passes through the polarization converter from the y direction, it is reflected to the x direction orthogonal to it, thus realizing the polarization conversion function.

For convenience of discussion, we refer to the unit of the PCM stated before as the "0" unit, as shown in Figure 3(a) [28]. According to the principle of the Pancharatnam-

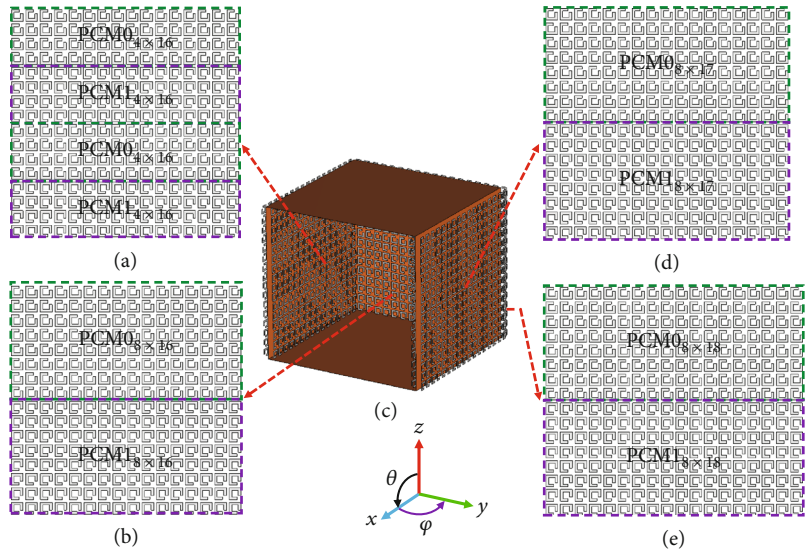

FIGURE 5: (a) The PCM loaded at the inner side of the cavity's two sidewalls. (b) The PCM loaded at the bottom of the inner side of the cavity. (c) The overall schematic of the cavity loaded with PCM. (d) The PCM loaded at the two sidewalls of the cavity's outer side. (e) The PCM loaded at the bottom of the cavity's outer wall.

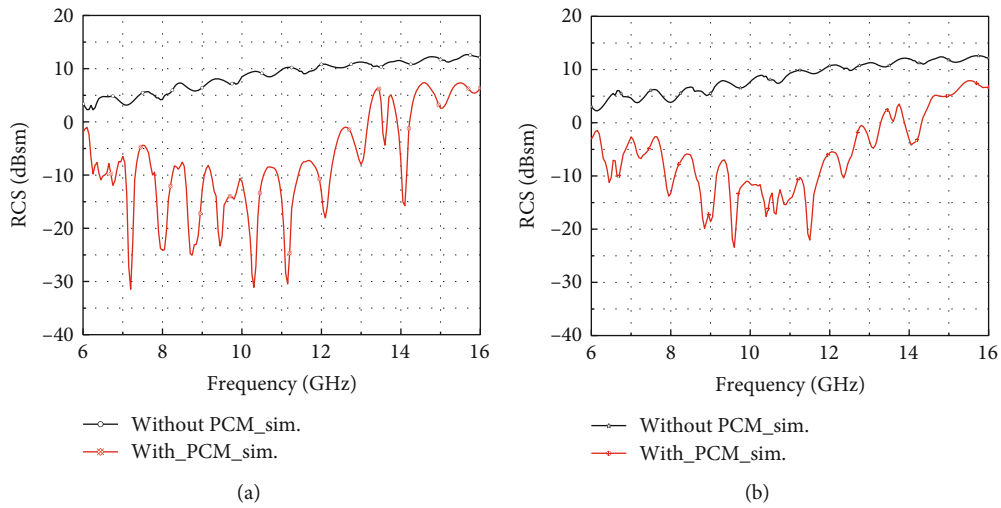

FIGURE 6: Simulated RCS of the cavity with and without PCM at different frequencies: (a) TE polarization and (b) TM polarization.

Berry (PB) geometric phase, the reflection phase of 2α is obtained when the metal pattern is rotated at α [35]. When the "0" unit is rotated clockwise by 90 degrees, we can obtain the "1" unit, as shown in Figure 3(b) [28], which has the same conversion characteristics as the "0" unit. As a result, the "0" unit is rotated 90 degrees clockwise to produce the "1" unit, which will have a 180° phase difference with the "0" unit, as illustrated in Figure 3(b) [28]. To further support the aforementioned point of view, we simulated the two units, respectively, and obtained their cross-polarization reflection coefficient and reflection phase. It can be seen from Figure 4(a) that the cross-polarization reflection coefficients of the "0" unit and the "1" unit are equal over the whole frequency band. The two structures can maintain a steady phase difference of 180 degrees throughout the whole frequency band, as can be seen in Figure 4(b). Namely, the reflection phase difference between the "0" and "1" units can be 180 degrees, and both units have the same conversion characteristics. Therefore, it can be further used for the design of scattering control.

The detailed design process of the low-RCS EOC is given after obtaining the "0" unit, which can be periodically arranged to form PCM0, and the "1" unit, which can be periodically arranged to form PCM1, combined with the principle of orthogonality. As shown in Figure 5(c), which is the overall schematic diagram of the cavity loaded with the PCM, the inner and outer sides of the cavity are both loaded on three sides. These planes are perpendicular to the incident surface. For the arrangement of the inner side of the cavity, by formula (2), we take the case of $m = 1$, that is,

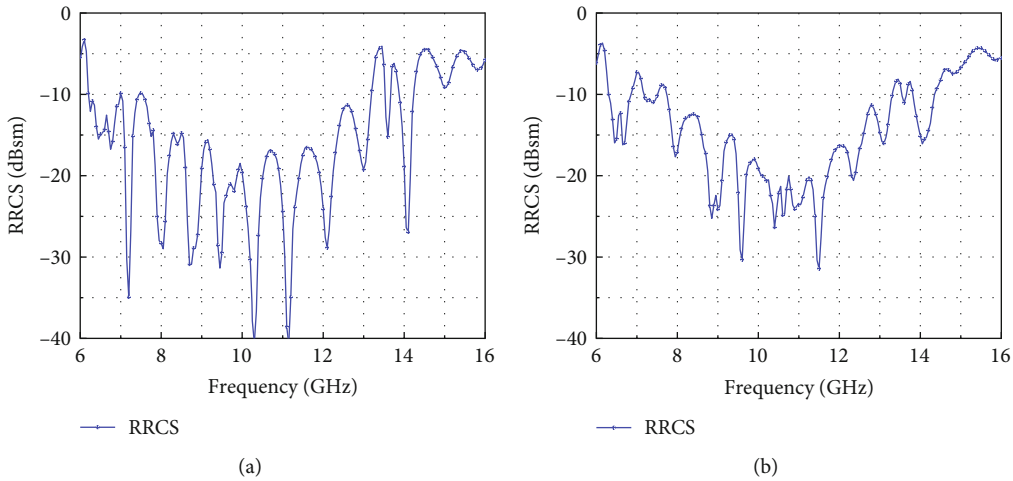

Figure 7: The RCS reduction at different frequencies: (a) TE polarization and (b) TM polarization.

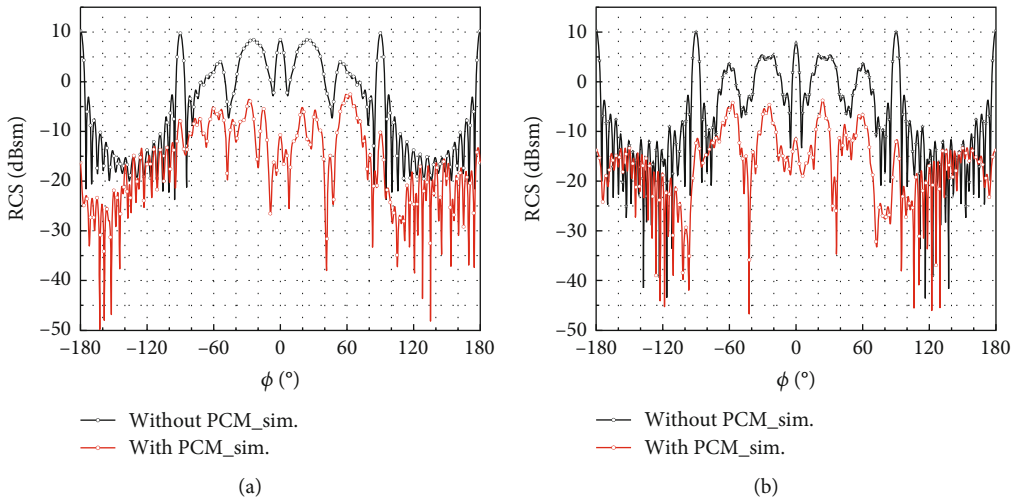

Figure 8: Simulated RCS of the cavity with and without PCM at 10 GHz at different azimuth angles: (a) TE polarization and (b) TM polarization.

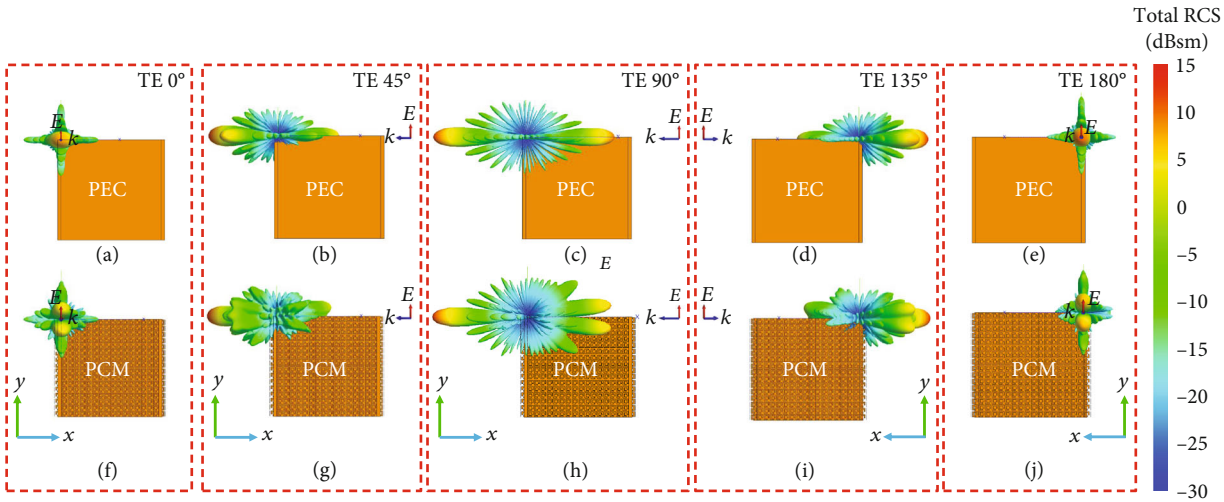

Figure 9: 3D bistatic scattering pattern of the cavity at 10 GHz at TE polarization, under an oblique incidence angle of (a) 0° without PCM, (b) 45° without PCM, (c) 90° without PCM, (d) 135° without PCM, (e) 180° without PCM, (f) 0° with PCM, (g) 45° with PCM, (h) 90° with PCM, (i) 135° with PCM, and (j) 180° with PCM.

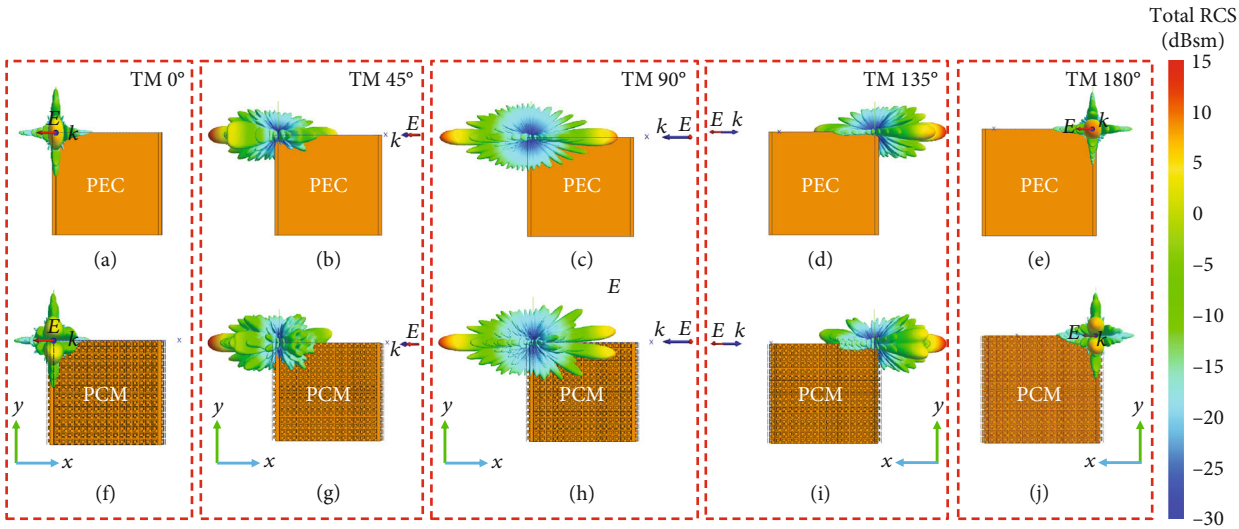

Figure 10: 3D bistatic scattering pattern of the cavity at 10 GHz at TM polarization, under an oblique incidence angle of (a) 0° without PCM, (b) 45° without PCM, (c) 90° without PCM, (d) 135° without PCM, (e) 180° without PCM, (f) 0° with PCM, (g) 45° with PCM, (h) 90° with PCM, (i) 135° with PCM, and (j) 180° with PCM.

$dp = 2dq$. As seen in Figure 5(a), the PCM loaded at the inner side of the cavity's two sidewalls is parallel to the *xoz* plane. It is made up of $PCM0_{4\times16}$, a supercell made up of 4 × 16 "0" elements, and $PCM1_{4\times16}$, a supercell made up of 4 × 16 "1" elements, placed alternately. In Figure 5(b), the PCM loaded at the bottom of the inner side of the cavity is parallel to the *yoz* plane. It consists of $PCM0_{8\times16}$, which is a supercell composed of 8 × 16 "0" elements, and $PCM1_{8\times16}$ arranged, which is a supercell composed of 8 × 16 "1" elements, alternately. In terms of the configuration of the cavity's exterior, according to formula (3), we take the case of $m = 1$, namely, $dp = dq$. In Figure 5(d), the PCM loaded at the two sidewalls of the cavity's outer side is parallel to the *xoz* plane. It is assembled from $PCM0_{8\times17}$, an arrangement of a supercell made up of 8 × 17 "0" units, and $PCM1_{8\times17}$, a supercell made up of 8 × 17 "1" units. Similarly, the PCM loaded at the bottom of the cavity's outer wall is parallel to the *yoz* plane in Figure 5(e). It is formed by $PCM0_{8\times18}$, a supercell generated of 8 × 18 "0" cells, and $PCM1_{8\times18}$, a supercell composed of 8 × 18 "1" cells, placed alternately. To prevent the pattern of the basic unit from being obscured, the thickness of the air medium in the middle of the metasurface is considered. Therefore, the size of the designed metal cavity as a control group is 160 mm × 160 mm × 165.5 mm. The cavity's dimensions become 160 mm × 171 mm × 182 mm when loaded with the metasurface.

The simulation results by Feko software with the multilevel fast multipole method (MLFMM) method are shown in Figure 6 when $\theta = 90^\circ$ and $\phi = 0^\circ$ under the incidence of TM polarized and TE polarized waves. We can see from Figures 6(a) and 6(b) that the cavity loaded with PCM has the effect of reducing RCS from 6 GHz to 16 GHz under TE and TM polarization. Under TE and TM polarization, the RCS reduction value after the cavity has been loaded with PCM is further shown in Figure 7. Under TE polarization, it achieves a -3 dB RCS reduction between 6 GHz and 16 GHz and a 10 dB decrease between 6.3 GHz and 13.2 GHz with fractional bandwidths of 70.77%, as shown in Figure 7(a). When TM polarization occurs, a -3 dB RCS

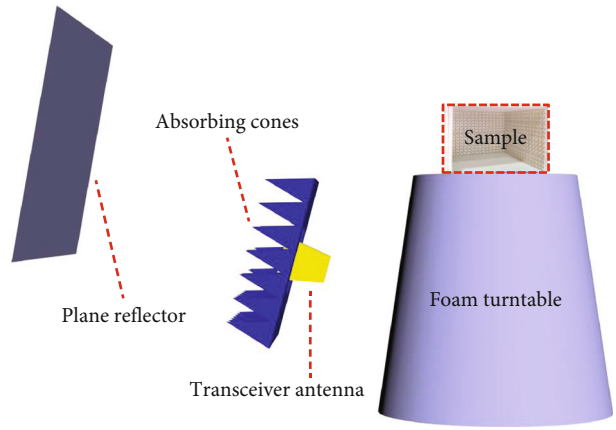

Figure 11: Schematic diagram of the experimental setup.

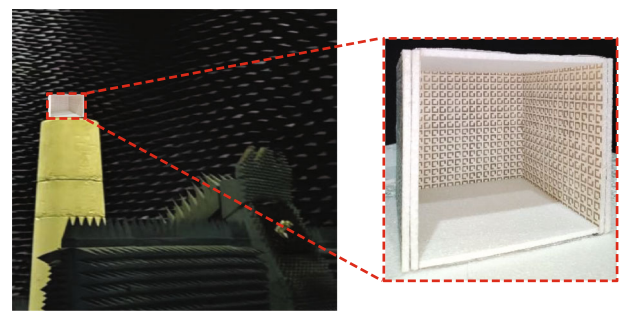

Figure 12: The schematic of the sample in the anechoic chamber and the insert map are photographs of the sample.

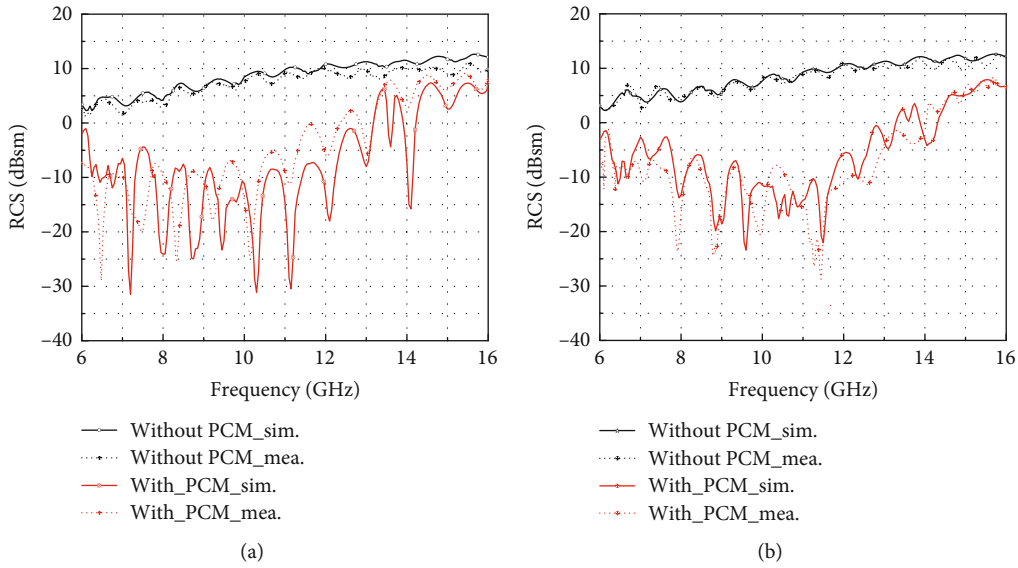

Figure 13: Simulated and measured RCS of the cavity with and without PCM at different frequencies: (a) TE polarization and (b) TM polarization.

reduction is attained between 6 GHz and 16 GHz, notably when a 10 dB reduction is attained between 7.8 GHz and 13.4 GHz with fractional bandwidths of 52.83%, as demonstrated in Figure 7(b). The results mentioned above demonstrate that the proposed low-RCS cavity structure loaded with PCM has broadband RCS reduction performance.

To further explore the ultra-wide-angle performance, the cavity is simulated before and after loading PCM at 10 GHz. When θ is 90° and ϕ changes from -180° to 180°, the simulation results for TE polarization and TM polarization are shown in Figure 8. Under TE and TM polarization, the low-RCS cavity has a very excellent RCS reduction between -180° and 180° after loading the PCM, as Figures 8(a) and 8(b) show. The aforementioned findings demonstrate the ultra-wide-angle RCS reduction performance of the proposed low-RCS cavity structure loaded with PCM. In conclusion, the low-RCS cavity structure loaded with PCM suggested in this paper exhibits excellent performance for both broadband and ultra-wide-angle RCS reduction under TE and TM polarization.

To further evaluate the performance of the RCSR, the 3D bistatic scattering pattern of the cavity with and without PCM is simulated. When the operation frequency is 10 GHz and the incident angle is 0°, 45°, 90°, 135°, and 180° under TE polarization and TM polarization, the result is shown in Figures 9 and 10, respectively. The scattered energy of the cavity without PCM is focused in the main lobe, as shown in Figures 9(a)–9(e). In contrast, when PCM is loaded, the main lobe separates and its strength decreases significant strength, as shown in Figures 9(f)–9(j). The main lobe of the cavity with PCM is successfully reduced in accordance with energy conservation theory. The simulation results in Figure 10 are similar to those in Figure 9. It is once again demonstrated that the designed low-RCS cavity with PCM has the characteristic of RCS reduction.

3. Experimental Results

To validate the accuracy and validity of the simulation design, we prepared experimental samples and tested them in the anechoic chamber. The experimental setup diagram is shown in Figure 11. The monostatic RCS test system includes a plane reflector, a vector network analyzer, a transceiver antenna, and a foam turntable. The reflector expands the electromagnetic waves' propagation distance. The electromagnetic wave that the measured object was irradiated with is nearly a plane wave, which satisfies the RCS test's requirements for far-field conditions. The experimental samples are placed on the turntable. By rotating the turntable, the omnidirectional monostatic RCS test may be carried out because the transceiver antenna's position is fixed. To obtain the metal pattern, we employ screen printing technology to print PCM on aramid paper with silver paste. The air medium layer in the middle is replaced by ROHACELL HF 51 foam ($\varepsilon_r = 1.05$ and tan $\delta = 0.0017$). Aluminum foil is pasted on the back of the foam as a metal ground plate. Our experimental sample diagram is displayed in Figure 12. The experimental sample is 160 mm × 171 mm × 182 mm in total.

As depicted in Figure 13, the simulation and measurement results of the low-RCS cavity under TE and TM polarization are presented. The outcomes of TE polarization and TM polarization are shown in Figures 13(a) and 13(b), respectively. As can be observed from Figure 13, the measurement results and simulation results are mostly in accord, and the 10 dB reduction bandwidth range is also in good agreement. This indicates that the PCM can be utilized to design the cavity to accomplish broadband RCS reduction. The simulation and experimental findings of the low-RCS cavity at 10 GHz, at various azimuth angles, are depicted in Figure 14. Figures 14(a) and 14(b) display the results of TE and TM polarization, respectively. From Figure 14, it is

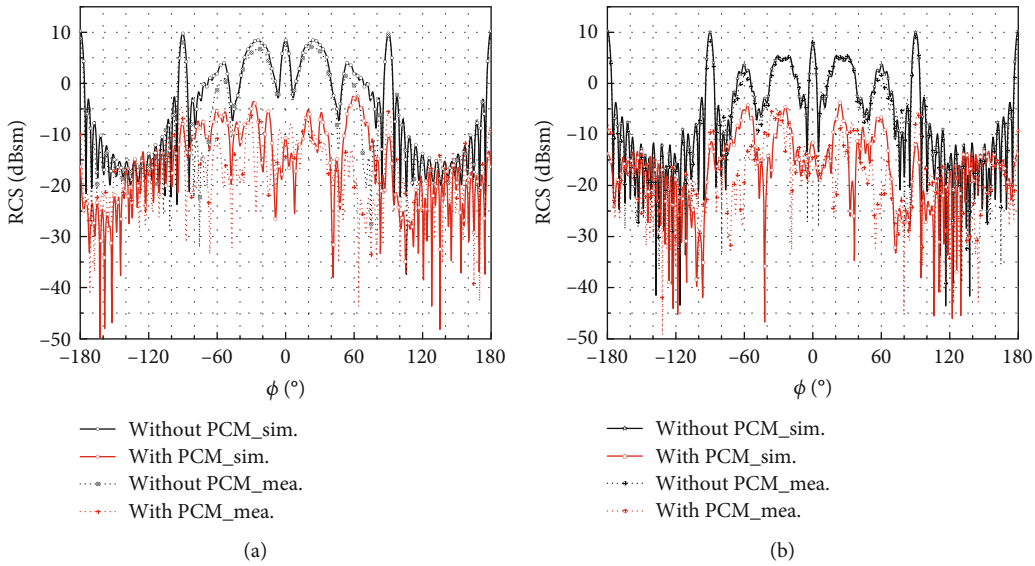

Figure 14: Simulated and measured RCS of the cavity with and without PCM at 10 GHz at different azimuth angles: (a) TE polarization and (b) TM polarization.

Table 1: Comparison with other previous work.

Ref.	Type	RCS reduction frequency band (GHz)	Fractional bandwidth (%)	Wide-angle performance (°)
[9]	Shape optimization	0.3, 1.2, 4.8	—	90-180
[16]	Radar absorbing coatings	10	—	-40~40
[17]	Radar absorbing material	2.4~4.8	66.67	90~180
[20]	Absorber	10	—	0, 15, 30, 45, 60
[23]	Random coding metasurfaces	8, 9, 10, 11, 12	—	10~80
This work	PCM	6.3~13.2 (for TE polarization); 7.8~13.4 (for TM polarization)	70.77 (for TE polarization); 52.83 (for TM polarization)	-180~180 (for TE and TM polarization)

obvious that the experiment findings and simulation results, from -180° to 180°, are essentially in agreement. This shows that the RCS reduction of the ultrawide angle can be accomplished by employing the PCM to design the cavity. From the comparison results of simulation and experiment, it can be seen that there are some differences between the two. These differences can primarily be attributed to the following factors: There is a certain error in the cutting process due to the large foam particles, and the relative dielectric constant of foam is close to but not equal to 1 within the tested frequency range; the pattern uses silver paste, which is easily oxidized and causes the performance to change. The ideal plane wave is used in the simulation, while the spherical wave generated by the horn antenna radiation is used in the experiment, which can be approximated as a plane wave in the far field. The experiment results demonstrate once again the viability and effectiveness of employing PCM to achieve broadband and ultra-wide-angle RCS reduction of the cavity.

The performance of our design is compared with the reported literature works, and the comparison is shown in Table 1. It can be seen from Table 1 that our work offers wideband and ultra-wide-angle RCS reduction compared to others reported work.

4. Conclusion

In conclusion, we have demonstrated a broadband and ultra-wide-angle RCS reduction approach for the EOC loaded with the PCM. The PCM construct, composed of a collection of polarizing reflectors, is loaded onto the inner and outer walls of the cavity in accordance with the array theory and the orthogonality principle to produce a 10 dB RCS reduction over 6.3 GHz to 13.2 GHz with fractional bandwidths of 70.77% for TE polarization and 7.8 GHz to 13.4 GHz with fractional bandwidths of 52.83% for TM polarization under normal incidence. The RCS performances under wide-angle incidence are also considered, and the ultra-wide-angle RCS reduction from -180° to 180° is achieved. The simulated and measured results are good consistent over the entire frequency range. The orthogonality principle is effective for controlling the scattering of electromagnetic waves from complex targets such as EOC, dihedral angle, and trihedral angle. To the best of our

knowledge, this is the first time the PCM, which is composed of a number of polarizing reflectors, has been employed to reduce the RCS of the EOC in both wideband and ultrawide angle. This approach, which is straightforward, efficient, and inexpensive, has a wide range of potential applications in the cavity's RCS reduction design. Overall, our research provides valuable insights and opens up new possibilities for reducing detectability in radar systems.

Data Availability

Data underlying the results presented in this paper are not publicly available at this time but may be obtained from the authors upon reasonable request.

Conflicts of Interest

The authors declare no conflicts of interest.

Acknowledgments

This work was supported by the National Natural Science Foundation of China (no. 52021001 and 51972046) and "111" Center (no. B13042) and partly supported by the Program for Changjiang Scholars and Innovative Research Team in University (PCSIRT).

References

[1] E. F. Knott, J. F. Shaeffer, and M. T. Tuley, *Radar Cross Section*, Artech House, Inc., Norwood, MA, 1993.

[2] Y. Li, J. Huang, S. Hong, Z. Wu, and Z. Liu, "A new assessment method for the comprehensive stealth performance of penetration aircrafts," *Aerospace Science and Technology*, vol. 15, no. 7, pp. 511–518, 2011.

[3] B. Zohuri, *Radar Energy Warfare and the Challenges of Stealth Technology*, Springer, 2020.

[4] R.-C. Chou, *Reduction of the Radar Cross Section of Arbitrarily Shaped Cavity Structures*, University of Illinois at Urbana-Champaign, 1987.

[5] H. Ling, R.-C. Chou, and S.-W. Lee, "Shooting and bouncing rays: calculating the RCS of an arbitrarily shaped cavity," *IEEE Transactions on Antennas and Propagation*, vol. 37, no. 2, pp. 194–205, 1989.

[6] H. T. Anastassiu, "A review of electromagnetic scattering analysis for inlets, cavities, and open ducts," *IEEE Antennas and Propagation Magazine*, vol. 45, no. 6, pp. 27–40, 2003.

[7] H. Ammari, G. Bao, and A. W. Wood, "Analysis of the electromagnetic scattering from a cavity," *Japan Journal of Industrial and Applied Mathematics*, vol. 19, no. 2, pp. 301–310, 2002.

[8] G. Bao and J. Lai, "Radar cross section reduction of a cavity in the ground plane," *Communications in Computational Physics*, vol. 15, no. 4, pp. 895–910, 2014.

[9] G. Bao and J. Lai, "Optimal shape design of a cavity for radar cross section reduction," *SIAM Journal on Control and Optimization*, vol. 52, no. 4, pp. 2122–2140, 2014.

[10] Y.-D. Kim, H. Lim, J.-H. Han, W.-Y. Song, and N.-H. Myung, "RCS reduction of open-ended circular waveguide cavity with corrugations using mode matching and scattering matrix analysis," *Progress In Electromagnetics Research*, vol. 146, pp. 57–69, 2014.

[11] J. W. Moll and R. G. Seecamp, "Calculation of radar reflecting properties of jet engine intakes using a waveguide model," *IEEE Transactions on Aerospace and Electronic Systems*, vol. -AES-6, no. 5, pp. 675–683, 1970.

[12] K. K. Chan and S. Wong, "Accurate RCS prediction of electrically large jet inlets and engines," in *Twelfth International Conference on Antennas and Propagation, 2003 (ICAP 2003). (Conf. Publ. No. 491)*, pp. 253–256, Exeter, UK, 2003.

[13] H. T. Anastassiu, J. L. Volakis, D. C. Ross, and D. Andersh, "Electromagnetic scattering from simple jet engine models," *IEEE Transactions on Antennas and Propagation*, vol. 44, no. 3, pp. 420-421, 1996.

[14] C. Lee and S.-W. Lee, "RCS of a coated circular waveguide terminated by a perfect conductor," *IEEE Transactions on Antennas and Propagation*, vol. 35, no. 4, pp. 391–398, 1987.

[15] E. F. Knott, J. F. Schaeffer, and M. T. Tulley, *Radar Cross Section*, SciTech Publishing, 2004.

[16] G. Xiang, S. Yong-Qiang, Y. Qing-Zhen, and C. Li-Hai, "Electromagnetic scattering characteristics of double S-shape exhaust nozzle with different coating medium parts," *Acta Physica Sinica*, vol. 64, no. 2, article 024103, 2015.

[17] G. Bao and J. Lai, "Radar cross section reduction of a cavity in the ground plane: TE polarization," *Discrete & Continuous Dynamical Systems-Series S*, vol. 8, no. 3, pp. 419–434, 2015.

[18] W.-H. Choi, T.-I. Kim, and W.-J. Lee, "Broadband radar absorbing sandwich composite with stable absorption performance for oblique incidence and its application to an engine duct for RCS reduction," *Advanced Composite Materials*, vol. 30, no. 1, pp. 76–90, 2021.

[19] F. Chen, J. Zhu, and W. Zhang, "Topology optimization for the layout design of radar absorbing coatings in cavities," *Structural and Multidisciplinary Optimization*, vol. 65, no. 9, p. 250, 2022.

[20] S. Bhattacharya and K. V. Srivastava, "Characterization and reduction of bistatic radar cross section of hollow cylindrical cavity," in *2022 IEEE USNC-URSI Radio Science Meeting (Joint with AP-S Symposium)*, pp. 42-43, Denver, CO, USA, July 2022.

[21] M. Paquay, J.-C. Iriarte, I. Ederra, R. Gonzalo, and P. de Maagt, "Thin AMC structure for radar cross-section reduction," *IEEE Transactions on Antennas and Propagation*, vol. 55, no. 12, pp. 3630–3638, 2007.

[22] F. Yuan, G.-M. Wang, H.-X. Xu, T. Cai, X.-J. Zou, and Z.-H. Pang, "Broadband RCS reduction based on spiral-coded metasurface," *IEEE Antennas and Wireless Propagation Letters*, vol. 16, pp. 3188–3191, 2017.

[23] Y. Zhou, Y. Yan, J. Xie et al., "Broadband RCS reduction for electrically-large open-ended cavity using random coding metasurfaces," *Journal of Physics D: Applied Physics*, vol. 52, no. 31, article 315303, 2019.

[24] J. Su, W. Li, M. Qu et al., "Ultrawideband RCS reduction metasurface based on hybrid mechanism of absorption and phase cancellation," *IEEE Transactions on Antennas and Propagation*, vol. 70, no. 10, pp. 9415–9424, 2022.

[25] M. Qu, C. Zhang, J. Su, J. Liu, and Z. Li, "Extremely wideband and omnidirectional RCS reduction for wide-angle oblique incidence," *IEEE Transactions on Antennas and Propagation*, vol. 70, no. 8, pp. 7288–7293, 2022.

[26] F. Yuan, Q. Chen, Y. Zheng, and Y. Fu, "Dual-mechanism absorptive metasurface with wideband 20 dB RCS reduction," *Crystals*, vol. 12, no. 4, p. 493, 2022.

[27] Q. He, J. Xie, Q. Liu et al., "A novel method for the low-detectable dihedral corner utilizing phase gradient metasurface based on phase cancellation mechanism," *The Applied Computational Electromagnetics Society Journal (ACES)*, vol. 38, no. 4, pp. 269–276, 2023.

[28] Q. He, H. Chen, Q. Liu et al., "Ultra-wideband and wide-angle RCS reduction of a concave structure based on a chessboard polarization conversion metasurfaces," *Journal of Physics D: Applied Physics*, vol. 57, no. 3, article 035104, 2024.

[29] M. Long, W. Jiang, and S. Gong, "Wideband RCS reduction using polarization conversion metasurface and partially reflecting surface," *IEEE Antennas and Wireless Propagation Letters*, vol. 16, pp. 2534–2537, 2017.

[30] Y. Shi, H. X. Meng, and H. J. Wang, "Polarization conversion metasurface design based on characteristic mode rotation and its application into wideband and miniature antennas with a low radar cross section," *Optics Express*, vol. 29, no. 5, pp. 6794–6809, 2021.

[31] M. Guo, W. Wang, F. Hao, P. Huang, L. Gong, and X. Song, "Low RCS, broadband polarization conversion metasurface antenna based on reactance loading," *IEEE Transactions on Antennas and Propagation*, vol. 70, no. 12, pp. 11361–11374, 2022.

[32] Y. Shi, P. P. Chu, and Z. K. Meng, "Ultra-wideband hybrid polarization conversion-absorption metasurface with a transmission window and narrow transition bands," *Journal of Physics D: Applied Physics*, vol. 56, no. 9, article 095102, 2023.

[33] A. Y. Modi, M. A. Alyahya, C. A. Balanis, and C. R. Birtcher, "Metasurface-based method for broadband RCS reduction of dihedral corner reflectors with multiple bounces," *IEEE Transactions on Antennas and Propagation*, vol. 68, no. 3, pp. 1436–1447, 2020.

[34] J. Chatterjee, A. Mohan, and V. Dixit, "Ultrawideband RCS reduction of planar and conformal surfaces using ultrathin polarization conversion metasurface," *IEEE Access*, vol. 10, pp. 36563–36575, 2022.

[35] X. Ding, F. Monticone, K. Zhang et al., "Ultrathin Pancharatnam–Berry metasurface with maximal cross-polarization efficiency," *Advanced Materials*, vol. 27, no. 7, pp. 1195–1200, 2015.